Synergistic alignment of low aspect-ratio π-conjugated molecules enables exceptional UV-Vis-NIR polarization detection

Yingying Xue[1, $], Qiong Zuo[1, $], Qi Zhu[1], Yukun Li[1], Zilin Deng[2], Zibang Zhang[2], Zhiyuan Yang[3], Cheng Wang [4], Rui Zhang[5], Xianjie Liu[5], Jingang Zhong[2], Wenkai Zhong[3, *], Lei Ying[3, *], Wanzhu Cai[1, *]

[1] Siyuan Laboratory, Guangdong Provincial Engineering Technology Research Center of Vacuum Coating Technologies and New Energy Materials, Department of Physics, College of Physics & Optoelectronic Engineering, Jinan University, Guangzhou 510632, P. R. China.

E-mail: wzhcai@jnu.edu.cn

[2] Department of Optoelectronic Engineering, College of Physics & Optoelectronic Engineering, Jinan University, Guangzhou 510632, P. R. China.

[3] Institute of Polymer Optoelectronic Materials and Devices, State Key Laboratory of Luminescent Materials and Devices, South China University of Technology, Guangzhou 510640, P. R. China.

E-mail: msleiying@scut.edu.cn, wkzhong@scut.edu.cn

[4] Advanced Light Source, Lawrence Berkeley National Laboratory, Berkeley, CA 94720, United States.

[5] Laboratory of Organic Electronics, Department of Science and Technology, Linköping University, Norrköping 60174, Sweden.

[$] These authors contribute equally.

Keywords:

polarization-sensitive photodetector, non-fullerene small-molecule, optical anisotropy, self-assembly, thermal annealing

Abstract:

Polarization detection enhances signal contrast and is widely utilized in diverse advanced applications. An ongoing challenge is the development of high-performance polarization-sensitive photodetectors based on optically anisotropic organic semiconductors, particularly in the near-infrared (NIR) region. While uniaxially aligned π-conjugated polymers with high aspect ratios exhibit strong linear dichroism and have shown promise, their limited NIR performance and-heavy reliance on polymer material now represent critical limitations. Here, we report a breakthrough in achieving giant linear dichroism and exceptional polarization detection with low-aspect ratios (AR) non-fullerene small-molecule (NFSM) acceptors, extending polarization sensitivity from the ultraviolet-visible to the NIR range. We demonstrate an impressive dichroic ratio of 27.1 at 605 nm and 12.0 at 780 nm. The maximum polarization photocurrent ratio is 11.2 at 780 nm under parallel versus perpendicular polarized light. This unprecedented performance originates from synergistic molecular alignment, wherein NFSMs significantly enhance the uniaxial orientation of both the polymer matrix and the NFSMs themselves during self-assembly and thermal annealing. Besides, we showcase such a linear-polarization-sensitive photodetectors (LPS-PDs) in generating degree-of-linear-polarization imaging. Our work establish NFSMs as a viable material system for next-generation of organic LPS-PDs and provides fundamental insights into structural origins of polarization sensitivity in low-AR organic semiconductors.

1.Introduction

Polarization-sensitive photodetectors hold extensive potential for advanced applications, including multidimensional optical imaging[1,2], optical communication[3,4], polarimetric imaging[5–9], and so forth. A polarization-sensitive photodetector not only detect the intensity of incoming light but also resolve the direction of the light wave's oscillations. A promising method in designing of such device involves leveraging optoelectronic materials with intrinsic linear or circular dichroism, which enables linear or circular polarization sensitivity without the need for additional optical components[6,10]. This approach holds significant potential for enhancing performance and expanding the range of applications by fundamentally simplifying the device architecture.

Among the photo-sensitive materials with intrinsic linear dichroism, π-conjugated polymers are highly promising candidates for linear-polarization-sensitive photodetectors (LPS-PDs)[11]. These materials typically feature a high molecular aspect ratio (AR), leading to the uniaxial alignment of transition dipole moments through global orientation of their backbones at various length scales[12]. The chemical versatility of π-conjugated polymers allows for tunable spectral selectivity, mechanical flexibility, and biocompatibility, making them particularly compelling for LPS-PDs[13]. The primary performance metric of LPS-PDs is their sensitivity to the polarization direction of light, quantified as the ratio of maximum to minimum photocurrent values, consistent with to the maximum and minimum absorbance of the photoactive layer, respectively. Therefore, maximizing the dichroism ratio (DR) is the prerequisite to achieve desirable performance. Early attempts to develop LPS-PD based on conjugated polymers were limited by low DR values, inherently constraining the performance[14–16]. Recent advancements have reported DR values up to 17 and polarization photocurrent ratio reaching 15[11,12], underscoring the significant potential of conjugated polymers in realizing efficient LPS-PDs. However, these performance metrics remain to be improved to meet the requirement of practical applications.

To date, while effects to achieve high DR in organic semiconductors have primarily focused on the alignment of high-AR polymers[17], π-conjugated small

molecules are equally critical in the realm of organic semiconductor[18–20]. In addition to their chemical versatility akin to polymers, certain advanced small molecules offer unique advantages, including strong absorption in the near-infrared (NIR) region[21] and mesoscopic long-range ordered molecular stacking[22], enabling higher light-conversion in NIR range and improved charge transport. Moreover, their clearly defined molecular structures facilitate purification and ensure batch-to-batch reproducibility, which are essential for high-performance photodetection. Despite these advantages, the polarization detection potential of small molecule has been significantly unexplored[23,24], and the structural origins of their polarization sensitivity remains poorly understood.

In this study, we demonstrate unprecedented polarization detection capabilities using non-fullerene small-molecule (NFSM), extending sensitivity from the ultraviolet-visible (UV-Vis) to the-NIR-range. More importantly, we unveil a synergistic alignment behavior of NFSM acceptors that enhances the optical anisotropy of donor polymers during self-assembly and thermal annealing (TA). This synergy drives a high degree of molecular and morphological orientation, effectively aligning both donor-and acceptor components across multiple scales and improving the performance of LPS-PDs. By incorporating the V-shaped NFSM Y6 into the conjugated polymer (P3HT) solution and employing a directional floating film transfer method, we establish the morphological foundation with highly molecular orientation, which is further promoted by-TA. The resulting films exhibits a remarkable DR of 27.1 at 605 nm (corresponding to P3HT absorption) and 12.0 at 780 nm (corresponding to Y6 absorption). Optimally oriented P3HT: Y6 blend films enable LPS-PDs with the maximum photocurrent ratio of 11.2 (parallel vs. perpendicular polarized light) under − 0.1 V bias, with high detectivities of 6.28×10^{13} Jones at 780 nm at a 210 Hz bandwidth in parallel direction. Finally, we present our NFSM-based LPS-PD for generating degree of linear polarization (DoLP) images.

2. Results and Discussion

2.1. Anisotropic optical absorption of NFSM

Various n-type non-fullerene small-molecules (NFSMs), including Y6, L8-BO, IEICO-4F, and COTIC-4F, exhibit exceptional anisotropic absorption in the uniaxially oriented bulk-heterojunction (BHJ) films when paired with donor polymers such as P3HT and PQT-C12. The full names of these materials are provided in the **Note S1** (Supporting Information). **Figure 1a** summarizes the chemical structures, UV-Vis-NIR absorption, and frontier orbital energy levels of these materials. Both P3HT and PQT-C12 show absorption in 350-700 nm, with maximum peaks near ~ 530 nm[25]. The NFSMs exhibit absorption in the NIR region, with peaks varying within 800-1000 nm[26–29]. Such complementary absorption between polymer donors and NFSMs provides broad spectral coverage from UV-Vis to NIR region. Meanwhile, the cascade alignments their energy levels ensure effective charge transfer between donor and acceptor, making them highly suitable for organic photodetectors.

Uniaxially oriented D: A BHJ films based on P3HT: Y6, P3HT: L8-BO, PQT-C12: IEICO-4F, and PQT-C12: COTIC-4F were prepared by directional floating film transfer method, followed by post-thermal annealing (TA) (**Figure 1b**). The anisotropic absorbance of these BHJ films are all measured under linearly polarized light, with the electric field oriented parallel and perpendicular to the alignment direction. **Figure 1c** presents polar plots of the absorbance for each oriented blend films at the characteristic wavelengths for their donor and acceptor absorption peaks. The solid lines represent fits to Malus' law: $A(\theta)=A_0\cos^2\theta$, where A is the absorbance, and θ is the angle between the polarized light and the reference direction. The excellent fits confirm the intrinsic linear dichroism for both polymers and NFSMs in the blend films. For all BHJ films, the absorbance of polarized light oriented perpendicular to the film's growth direction is maximized, indicating that the in-plane optical transition dipole moments of the polymers/NFSM are predominantly aligned in this direction[30]. This direction is denoted as the parallel direction (∥) in this study (marked in **Figure 1b**). Conversely, the absorption of polarized light in the perpendicular direction is minimized.

The linear dichroism is quantified using DR[24], defined as $A_{\parallel}/A_{\perp}$. Table S1 (Supporting Information) summarizes the optimized DR values for various BHJ film. Figure S1a (Supporting Information), presents the corresponding polarized absorption

spectra and spectral DR values. Among the studied films, the oriented P3HT:Y6 film (hereafter O-P3HT:Y6) achieved the highest DR of 27.1 at 605 nm, primarily due to the well-aligned P3HT chains. In the NIR region, the maximum DR was 12.0 at 780 nm, attributed to the oriented Y6 molecules. For blend systems based on other NFSMs, the DR values were 7.6 at 740 nm for L8-BO, 5.5 at 830 nm for IEICO-4F, and 2.6 at 760 nm for COTIC-4F. Since the absorption in this spectral range originates solely from the NFSMs, we can confirm that the pronounced linear dichroism is due to the well-aligned NFSMs. For a comparison with state-of-the-art performance, the DR of organic material-based LPS-PDs is summarized in Table S2 (Supporting Information)**.** Notably, our work not only achieves the highest DR values in the visible region[24,31], but also realizes high DR in the NIR range for the first time. Additional evidence supporting the NFSM alignment is provided by polarized light microscopy (Figure S2, Supporting Information) and a digital video shown in **Supplementary Video**.

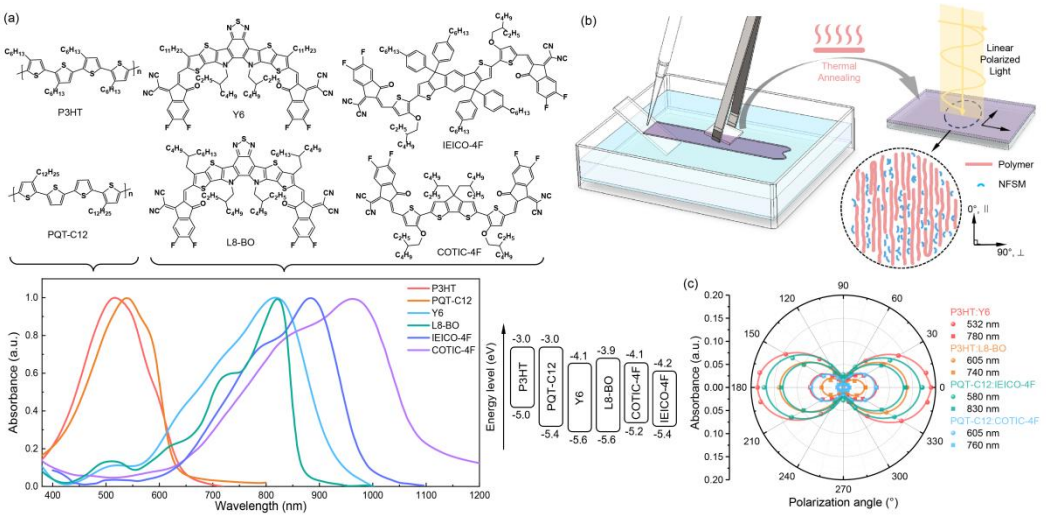

Figure 1. a) Chemical structure of the donor (P3HT and PQT-C12) and NFSMs (Y6, L8-BO, IEICO-4F, and COTIC-4F), their absorbance spectra, alongside their respective approximate energy levels. b) Schematic diagram of the fabrication process utilizing directional floating film transfer method and post-thermal annealing (TA). The interior of the circle illustrates the orientation of the polymer/NFSM is largely orthogonal to film growth direction. Adjacent to this is the definition of incident light with parallel and perpendicular polarization orientations. c) Polar plots depicting the absorbance of the BHJ film at two characteristic wavelengths corresponding to the donor and acceptor materials, each as a function of the linear polarization angle, with a fitting curve using

Malus' equation.

2.2. Synergistic alignment behavior of NFSM

To unveil the synergistic role that NFSMs played in enhancing the optical anisotropy of the donor polymer during self-assembly and TA treatment, O-P3HT:Y6 blend was used as the model system due to its most pronounced optical anisotropy. The structural features of P3HT and Y6 are detailed in **Note S2** (Supporting Information). We initially measured the polarized absorption spectra of O-P3HT:Y6 films at varying mixing ratios (Figure S3, Supporting Information). **Figure 2a** reveals that at the mixing ratio of 4:1, the DR values reach their maxima: 6.9 at 450 nm, 13.5 at 532 nm, and 11.5 at 780 nm. **Figure 2b** shows the characteristic peak positions for P3HT (λ_{P3HT}) and Y6 (λ_{Y6}) across different mixing ratios. For spectra measured by parallel-polarized light, λ_{P3HT} remains stable at ~532 nm for the 5:1 and 4:1 blend, indicating that low Y6 addition does not perturb the intrachain conjugation or interchain packing of P3HT. A detailed discussion of peak origins and variations is provided in the **Note S3** (Supporting Information). However, as the Y6 content increases beyond a 4:1 ratio, λ_{P3HT} shifts to shorter wavelengths, suggesting a reduction in conjugation length of the P3HT due to excessive Y6. In contrast, for perpendicularly polarized light, λ_{P3HT} undergoes a gradual red shift with increasingY6 concentration, reflecting subtle improvements in the ordering of P3HT chains along the perpendicular direction. For all mixing ratios, the λ_{P3HT} in the parallel polarized absorption is consistently at a longer wavelength compared to that in the perpendicular absorption, indicating that more P3HT chains (or segments) adopt an ordered along the parallel direction. The λ_{Y6} emerges around 780 nm at mixing ratios of 5:1 and 4:1, which can be attributed to relatively isolated Y6 molecules[32]. As the Y6 concentration increases, λ_{Y6} gradually red-shifts in both parallel- and perpendicular-polarized spectra, signaling the onset of Y6 aggregation, which coincides with the disruption of ordered alignment of P3HT.

Figure 2c, **d** summarize the DR values at 605 and 780 nm for films without (w/o) and with (w) TA at various annealing temperatures. To quantify the enhancement, a metric referred to as the "Ratio" ($= \frac{DR_w}{DR_{w/o}}$) was used, where $DR_{w/o}$ and DR_w represent

the DRs of the films without and with TA, respectively. At 605 nm, the Ratio reaches its peak average value of 2.5 at a TA temperature of 120 °C, with a similar trend observed at 780 nm. The optimal TA duration was determined to be 30 minutes (Figure S4, Supporting Information). The polarized absorption spectra and corresponding spectral DR of O-P3HT:Y6 films before and after 120 °C TA for 30 min are shown in **Figure 2e**. The parallel-polarized spectrum exhibits higher absorbance and a red-shifted P3HT peak with narrow, well-resolved features compared to the perpendicular-polarized spectrum, resulting in a maximum DR of 27.1 appears at 605 nm after TA. Such results suggest that in the parallel direction, P3HT chains achieve a higher degree of both intrachain and interchain order after TA, contributing to the improved optical anisotropy[33].

To highlight the role of Y6 in enhancing optical anisotropy during TA, we compared the polarized absorption spectra and spectral DR of oriented P3HT thin film (hereafter O-P3HT) treated under the same TA conditions (**Figure 2f**). Before TA, O-P3HT film has an absorption peak at 522 nm in the parallel-polarized spectrum and 493 nm in the perpendicular-polarized spectrum (Figure S5, Supporting Information). After TA, the main peak red-shifts to 530 nm with a shoulder at 601 nm in the parallel-polarized spectrum. However, the spectral DR remains low, with a maximum of ~3 at 605 nm. The DR at 605 nm of O-P3HT films under different TA temperatures shows limited enhancement, with a maximum 1.5-fold increase at 100 °C, compared to as-cast films (**Figure 2g**). The O-P3HT:L8-BO blends exhibit a 2-fold increase in DR at a lower TA temperature of 80 °C (**Figure 2h**), which could be attributed to the lower glass transition temperature (T_g) of L8-BO (~78 °C) compared to Y6 (~105 °C). The higher diffusion mobility of L8-BO near its T_g likely facilitates better molecular and chain segmental reorganization. These results highlight the critical role of NFSM molecular motion in assisting chain orientation during film processing, with their T_g playing a key role in optimizing molecular alignment and optical anisotropy[34–36].

We propose that in solution, a small amount of Y6 may acts like a plasticizer, disentangling P3HT chains and reducing pre-aggregation, thereby facilitating better alignment during self-assembly. The P3HT chains adopt a uniaxial orientation, with Y6

molecules interspersed and aligned along the same direction, forming a loosely ordered structure. Upon TA, the structure transitions into a more compact molecular packing, leading to enhanced P3HT ordering and Y6 aggregation. As the TA process lacks directional selectivity, aggregation occurs both along the primary orientation and in other directions (**Figure 2i**).

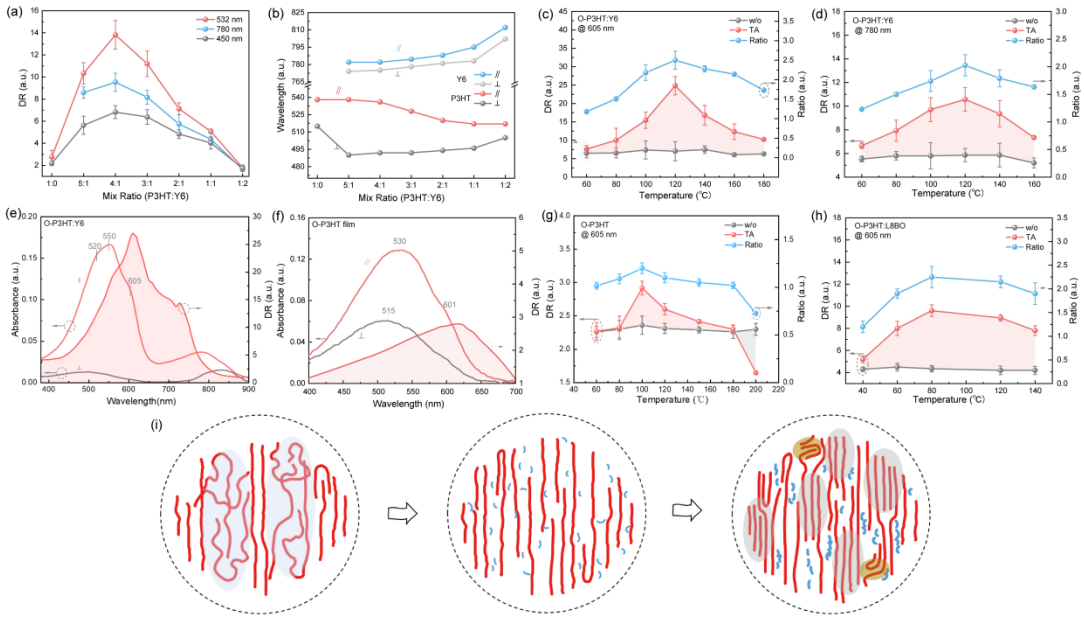

Figure 2. a) DRs of films with different mixed ratio of P3HT:Y6. b) The shift of absorption peaks from P3HT and Y6 in parallel and perpendicular direction with different mixing ratio. DR without (w/o) and with TA-treatment, along with the corresponding Ratio of the O-P3HT:Y6 film at c) 605 nm and d) 780 nm. The polarized absorption spectrum and spectral DR without and with optimized TA treatment of e) the O-P3HT:Y6 and f) the O-P3HT film. DR without and with TA treatment, along with the corresponding Ratio of the O-P3HT film at g) 605 nm and h) of the O-P3HT:L8-BO film at 605 nm. i) Molecular orientation model for O-P3HT:Y6 during self-assembly and subsequent TA process. The red and blue lines represent P3HT and Y6, respectively. The shaded region in the left figure highlights entangled P3HT in solution, while the shaded region in the right figure illustrates the well-packed and oriented P3HT domain due to TA, with blue and yellow colors indicating different orientations.

2.3. Morphological origins of optical anisotropy

Grazing incidence wide angle X-ray scattering (GIWAXS) was used to study the

crystalline packing in O-P3HT and O-P3HT:Y6 blend films. For comparison, spin-coated neat P3HT, Y6, and P3HT:Y6 film were also tested (Figure S6, Supporting Information). For oriented films, X-rays were directed parallel and perpendicular to the reference direction[37,38], as illustrated in Figure S7, Supporting Information. The resulting scattering images and sector-averaged *I-q* curves for in-plane (IP) and out-of-plane (OOP) directions are shown in **Figures 3a-d**, with detailed data provided in Table S3 (Supporting Information). For neat O-P3HT films probed by parallel X-rays, π-π stacking reflections at 1.67 $Å^{-1}$ appear in the IP direction, while (100), (200), and (300) lamellar reflections dominate in the OOP direction. When probed perpendicularly, the π-π stacking reflection in the IP direction diminishes significantly, whereas lamellar stacking reflections persist, indicating a preferential edge-on orientation of P3HT crystals with chain backbones aligned to the reference direction[39]. In O-P3HT:Y6 blends, the scattering patterns reveal that P3HT retains its edge-on orientation with chain alignment along the reference direction. However, no π-π stacking or (11-1) reflections from Y6 are observed, suggesting Y6 is amorphous in the blends. As the Y6 content increases (with mixing ratio varying from 1:0 to 2:1), the π-π stacking reflections of P3HT shift to higher q values, corresponding to a tightening of d-spacing from 3.76 Å to 3.64 Å (**Figure 3e**). This is accompanied by an increase in peak area and a reduction in crystalline coherence length (CCL), indicating enhanced crystallinity but greater packing dislocations. These results suggest that Y6 may acts as a plasticizer during film formation, facilitating P3HT chain mobility and enabling the formation of more refined crystals with tighter molecular packing[40,41].

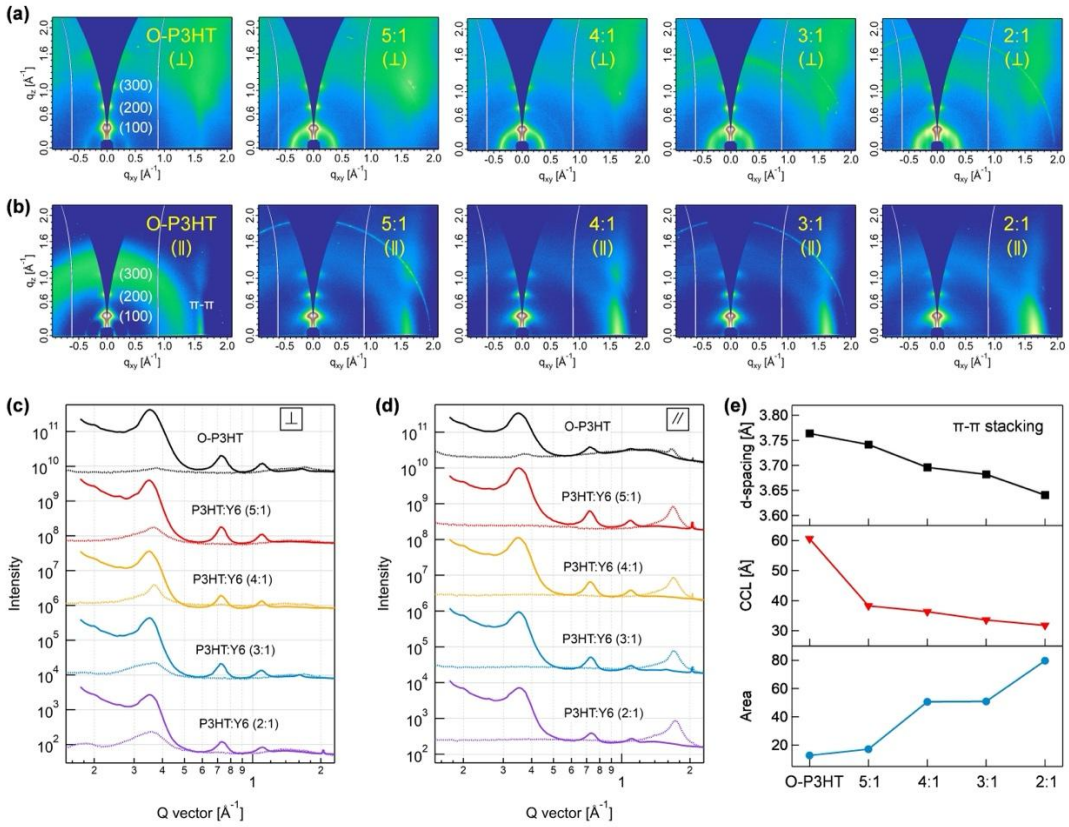

Figure 3. a-b) GIWAXS patterns of neat O-P3HT and O-P3HT:Y6 blend films with varying mixing ratios, measured with X-ray perpendicular (perp.) and parallel (para.) to the reference direction. c-d) GIWAXS averaged I-q curves in the IP (dotted lines) and OOP (solid lines) directions of the 2D patterns. e) Summary of d-spacing, CCL, and area of π-π stacking reflections of thin films.

The enhanced P3HT crystallization significantly impacts the film morphology. Atomic force microscopy (AFM) height images reveal that the O-P3HT film displays a fibrillar-liked morphology, consistent with P3HT's intrinsic tendency for fibrillization (**Figure 4a**). TA promotes the formation of highly oriented structures within the film, indicating that the directional floating processing offers a foundational morphological alignment, which TA further refines to enhance global orientation. In the O-P3HT:Y6 (4:1) blend film, and particularly in the TA, the oriented structures become more compact, elongated, and strongly aligned along the reference direction. This alignment correlates with the GIWAXS results (Figure S4, S8, Supporting Information), where π-π stacking reflections predominantly appear along the reference direction, suggesting that P3HT chains parallel to such oriented structures.

To further elucidate the role of Y6 in morphological transformation, C K-edge resonant soft X-ray scattering (RSoXS) was employed to analyze the O-P3HT:Y6 blend films. The 2D RSoXS patterns show pronounced anisotropic signals, particularly along the reference direction (**Figure 4b**). Such scattering anisotropy is unaffected by the X-ray electric field orientation, indicating a globally oriented morphology. **Figure 4c** shows the RSoXS *I-q* curves at 284.8 eV, sector-averaged along parallel and perpendicular directions to the reference direction. Across all blend films, the scattering interferences occur at higher q values in the perpendicular direction compared to the parallel direction, reflecting distinct characteristic length scales. We attribute the shorter d-spacing in the perpendicular direction to distances between the oriented structures, while the larger d-spacing in the parallel direction corresponds to inter-crystal distances of P3HT. Fitting results show that both such distances are minimized for the 4:1 mixing ratio, indicating the formation of the most compact oriented crystals and structures in this film.

The combined findings from GIWAXS, AFM, and RSoXS demonstrate that Y6 facilitates P3HT crystallization, promoting the formation of compact, ordered, and oriented structures. This behavior creates high aspect-ratio regions between fibrils, effectively confining amorphous Y6 molecules and enabling their oriented arrangement. This outcome aligns with the molecular orientation model previously proposed (**Figure 2i**). Such multiscale structural organization is likely the primary morphological origin of the high DR values observed for both P3HT and Y6.

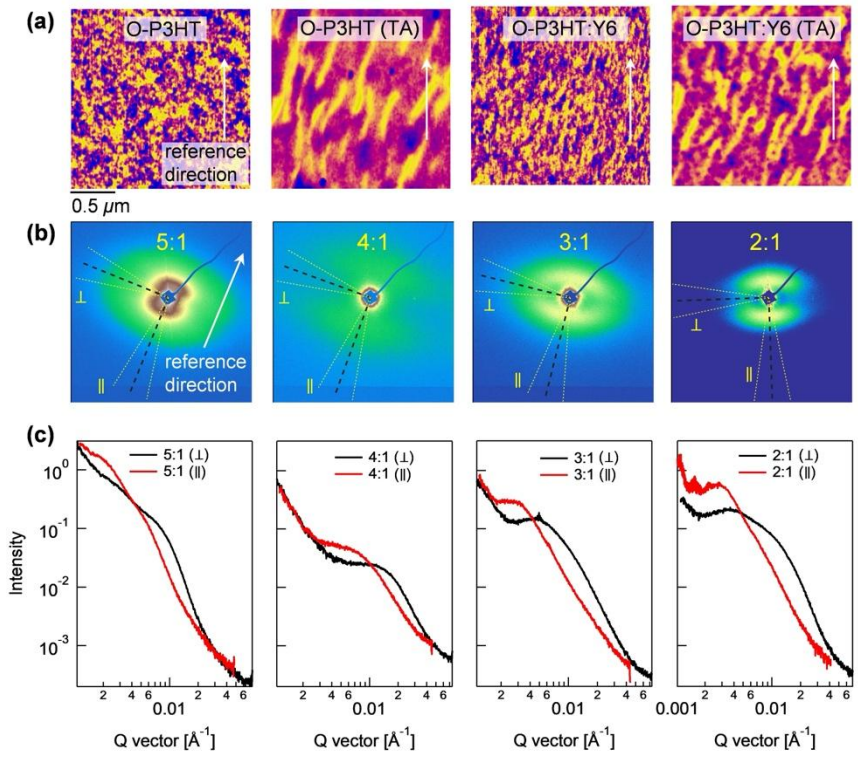

Figure 4. a) AFM height images of O-P3HT and O-P3HT:Y6 films treated without and with TA. b) RSoXS patterns of O-P3HT:Y6 blend films with varying mixing ratios. c) RSoXS I-q curves of O-P3HT:Y6 blend films averaged perpendicular (perp.) and parallel (para.) to the reference direction.

2.4. Performance and imaging application of LPS-PD

The O-P3HT:Y6 (4:1) blend film, showing the optimal DR value, was integrated into LPS-PDs with architecture ITO/ZnO/PFN-Br/O-P3HT:Y6/MoO_3/Ag. The energy levels of each layer are shown in **Figure 5a**,**b**. Polarization-dependent current density-voltage (*J-V*) curves under illumination at 2.43 mW/cm² (780 nm), 3.19 mW/cm² (605 nm), and in the dark are presented in **Figure 5c**. Distinct reverse-bias responses between parallel and perpendicular polarized light at both wavelengths arise from the anisotropic absorption of P3HT and Y6 at 605 nm and 780 nm, respectively. While P3HT contributes strong polarization detection in the visible range, Y6 enhances this sensitivity in the NIR region. Polar plots of the photocurrent at 780 nm **(Figure 5d)** fitted with Malus's law, align with the optical anisotropy of Y6, confirming that the polarization sensitivity of the device originates from the optical anisotropy of the O-P3HT:Y6 film (Figure 1c). At 780 nm, the device achieves the maximum photocurrent

ratio (polarization ratio) of 11.2 at -0.1 V bias. **Figure 5e** presents the polarization ratio of the LPS-PD under 780 nm parallel and perpendicular polarized light as a function of the P3HT:Y6 mixing ratio.

Responsivity spectra under white light at 0 V are shown in **Figure 5f**. At 0 V in parallel direction, the responsivity peaks at 0.024 A/W at 451 nm, with a shoulder at 0.024 A/W at 605 nm and 0.016 A/W at 780 nm, as calculated based on external quantum efficiency (EQE) data. **Figure 5g** illustrates the polarization ratio at -0.1 and -0.5 V based on the *J-V* curve. The responsivity under polarized light is derived from the equation $R = \frac{I_{ph}}{P_{in}} = \frac{I_{Photocurrent} - I_{Dark\ current}}{P_{in}}$, where the raw data can be found in Figure S9, Supporting Information. The responsivity under parallel-polarized light is 0.0121, 0.0058, 0.0051, and 0.0049 A/W at wavelengths of 605, 730, 780, and 800 nm under 0 V bias, respectively. In contrast, the responsivity under perpendicular-polarized light decreases to 7.5×10^{-3}, 9.9×10^{-4}, 3×10^{-4}, and 6.8×10^{-4} A/W at the same wavelengths. Thus, the corresponded responsivity ratio is 1.61, 5.86, 17.0, 7.2 under 605, 730, 780, 800 nm polarized light under 0 V bias, respectively. The responsivity under white light falls between the values measured under parallel and perpendicular polarized light. **Figure 5h** shows the specific detectivity (D^*) across the visible to NIR range. At 0 V and 210 Hz bandwidth, detectivity is 9.93×10^{13} Jones at 451 nm, 9.39×10^{13} Jones at 605 nm, and 6.28×10^{13} Jones at 780 nm in parallel direction. Additionally, the device demonstrates a -3 dB frequency of 3.1 kHz, rise and fall times of 7.34 and 9.34 μs, and a linear dynamic range (LDR) of 129.6 dB Figure S10 (Supporting Information). These attributes highlight the O-P3HT:Y6 based-LPS-PD as an efficient and versatile candidate for practical applications.

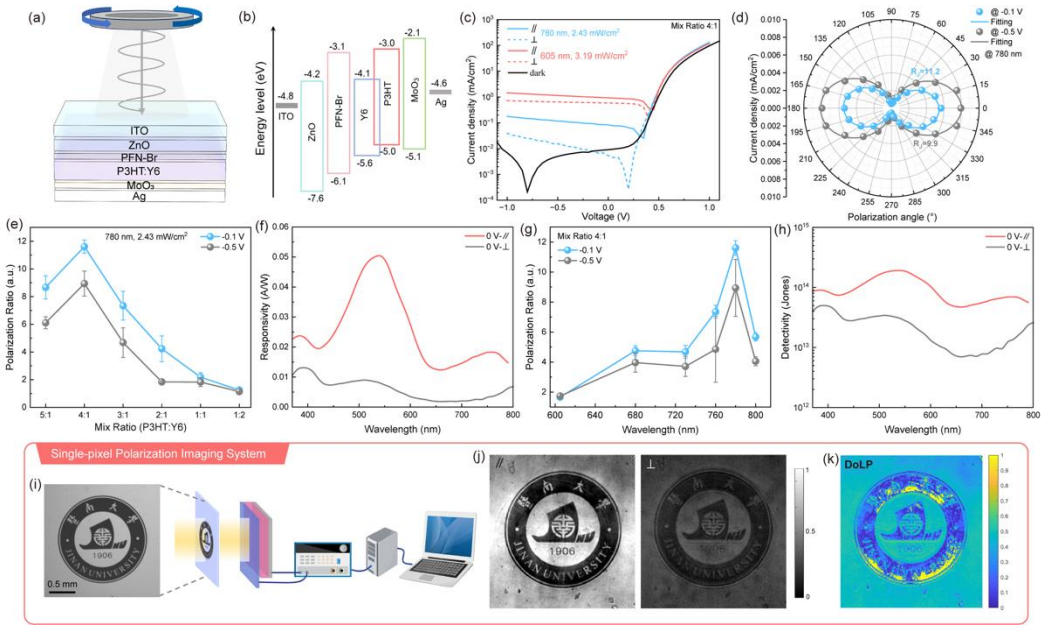

Figure 5. a) Device architecture of LPS-PD, and b) the approximate alignment of energy levels within the device. c) Polarization dependent *J-V* curve under 2.43 mW/cm² at 780 nm, 3.19 mW/cm² at 605 nm, and in dark. d) The polar plots of the photocurrent at 780 nm as a function of the linear polarization angle, under -0.1 and -0.5 V bias. e) The photocurrent ratio of the LPS-PD under 780 nm parallel and perpendicular polarized light is plotted as a function of the P3HT to Y6 mixing ratio. f) The polarization ratio of the LPS-PD under parallel and perpendicular polarized light is plotted as a function of the incident light wavelength at biases of 0 V. g) The polarization ratio of the LPS-PD from the visible to NIR region under -0.1 and -0.5 V bias. The calculated responsivity under parallel and perpendicular polarized light at 605, 730, 780, and 800 nm is represented by dots. h) The specific detectivity of the LPS-PD under 0 V bias at 10 Hz and 210 Hz test bandwidths. i) Schematic diagram of imaging system. j) Mapping 2D images at the polarization angles of 0° and 90°, respectively, using the LPS-PD based on O-P3HT:Y6 film (4:1) under white LED illumination and k) corresponding DoLP image.

To showcase the utility of LPS-PD, the O-P3HT:Y6 (4:1) device was integrated into a single-pixel microscopic imaging system[42]. The detailed imaging setup is shown in **Note S4** (Supporting Information). A mask fabricated with the logo of Jinan University was used as the target object (**Figure 5i**). The system used Fourier basis patterns to illuminate the target object, and the corresponding intensity of the

transmitted light was collected by the detector. By correlating the patterns and the single-pixel measurements, the target object image was reconstructed. Images acquired under illumination with different polarization orientations were reconstructed, with normalized response signal mapping images at parallel and perpendicular polarization demonstrating a signal intensity ratio of ~3 between the two conditions **(Figure 5j).** To enhance imaging quality, the degree-of-linear-polarization (DoLP) was calculated and visualized, which significantly reduces background noise and improves contrast compared to the raw signal mapping **(Figure 5k)**. By capturing and analyzing the polarization characteristics of light, DoLP imaging provides additional information unattainable by conventional methods, offering potential for application in scientific research, industrial processes, and healthcare[43].

3. Conclusion

For the first time, this study demonstrates that NFSMs with low structure AR can exhibit significant linear dichroism and exceptional polarization sensitivity. We reveal a synergistic alignment behavior of NFSMs during self-assembly and TA, which significantly modulates and enhances the polarization sensitivity of both π-conjugated polymers and the NFSMs themselves, extending the polarization sensitivity across the UV-Vis-NIR spectrum. Morphological analysis shows that Y6 suppress the P3HT pre-aggregation, promotes better chain alignment, and, after TA, results in more compact molecular packing with increased structural order. This research not only introduces a critical class of NFSM acceptor materials into polarization-sensitive optoelectronics, but also advance our understanding of the uniaxial alignment mechanisms of organic semiconductors.

4. Experimental Section

Materials: The materials utilized in this study included P3HT and PQT-12, both sourced from Luminescence Technology Co. Y6 and L8-BO were acquired from Volt-amp Optoelectronics Technology Co. and Derthon Optoelectronic Materials Science Technology Co., Ltd., respectively. $PC_{61}BM$ ([6,6]-phenyl-C61-butyric acid methyl

ester) (>99% purity) was procured from Xi'an Polymer Light Technology Co., while COTIC-4F and IEICO-4F were obtained from Organtec Ltd. The solvents used, including chloroform (>99% purity), anhydrous ethanol (>99.9% purity), chlorobenzene (>99% purity), and ethylene glycol (>99% purity), were supplied by Alfa Aesar. All materials were commercially available and used as received without further purification.

Device Fabrication and Characterizations: The photodetector devices were fabricated with ITO/Zno/PFNBr/BHJ/MoO_3/Ag, where the active area was 12.5 mm^2. ITO (indium tin oxide) substrates were sequentially cleaned with acetone, ethanol, and deionized water using ultrasonic treatment for 15 minutes each. A sol-gel ZnO (zinc oxide) precursor was spin-coated onto the ITO at 3000 rpm for 30 seconds, followed by thermally annealed at 200 °C for 30 minutes. After cooling to room temperature, the PFN-Br solution was spin-coated onto the ITO/ZnO at 2000 rpm for 30 seconds. The BHJ layer was then deposited via floating film transfer method in a fume hood. Finally, a 10 nm MoO_3 (molybdenum trioxide) and a 100 nm Ag (silver) top electrode was deposited by thermal evaporation in a glovebox filled with nitrogen.

Current density-voltage (*J-V*) curves were measured using a Keithley 2400 source meter. Angle-dependent photocurrent measurements across different wavelengths were conducted using a polarizer and a half-wave plate in a glovebox. The response spectrum was acquired using a QE-R test system (Enli Technologies, Inc.). Noise current was first amplified by a current pre-amplifier (SR 570) and then digitized by an Fast Fourier Transform **(**FFT) spectrum analyzer (Stanford Research, SR785).

General Characterizations: The UV-Vis-NIR absorption spectra were recorded using a Shimadzu UV-2600 spectrophotometer. Incident light polarization was controlled with a linear polarizer (Ocean Optics) positioned at the light exit, and the polarization direction was adjusted via a half-wave plate. Cross-polarized microscopic images were captured using a Nikon Eclipse LV100 POL microscope. AFM characterization was conducted using a Bruker INNOVA Atomic Force Microscope in tapping mode.

GIWAXS was performed at beamline 7.3.3 of the Advanced Light Source (ALS),

Lawrence Berkeley National Laboratory (LBNL). The incident X-ray energy was kept at 10 keV. Thin films were prepared on silicon wafers through the directional floating film transfer method or spin-coating. The X-ray beam was directed at an incidence angle of 0.16°, with a sample-to-detector distance of ~280 mm. Scattering patterns were recorded using a Pilatus 2M CCD detector with a 5-second exposure time.

RSoXS was conducted at beamline 11.0.1.2 of ALS, LBNL. The thin films were transferred onto silicon nitride windows for transmission-mode experiments. The X-ray electric field was kept horizontally polarized. Scattering images were captured using a Princeton Instrument PI-MTE CCD camera with a 5-second exposure time. The high-q range data (0.004-0.075 $Å^{-1}$) and low-q range data (0.001-0.02 $Å^{-1}$) were collected with sample-to-detector distance of 150 mm and 50 mm, respectively. The final I-q curves were obtained by merging the high-q and low-q data.

Supporting Information

Supporting Information is available from the Wiley Online Library or from the author.

Acknowledgements

This work was supported by Guangdong Basic and Applied Basic Research Foundation (2025A1515010028, 2024A1515030006, 2022B1515120008, 2024A1515010309), Fundamental Research Funds for the Central Universities (2023ZYGXZR097, 21624406), research project of the State Key Laboratory of Luminescent Materials and Devices at South China University of Technology (No. Skllmd-2024-23), and National Natural Science Foundation of China (U24A20304). GIWAXS and RSoXS were performed at beamlines 7.3.3 and 11.0.1.2 at the Advanced Light Source, a U.S. DOE Office of Science User Facility under contract no. DE-AC02-05CH11231.

Conflict of Interests

The authors declare no conflict of interest.

Data availability Statement

The data that generate the results of this study are available from the corresponding authors upon request.

References

[1] A. Pierre, A. Gaikwad, A. C. Arias, *Nature Photon* **2017**, *11*, 193.

[2] L. Li, W. Han, L. Pi, P. Niu, J. Han, C. Wang, B. Su, H. Li, J. Xiong, Y. Bando, T. Zhai, *InfoMat* **2019**, *1*, 54.

[3] P. Chvojka, A. Burton, P. Pesek, X. Li, Z. Ghassemlooy, S. Zvanovec, P. A. Haigh, *Opt. Lett., OL* **2020**, *45*, 2977.

[4] H. Wang, L. Liu, C. Lu, *Procedia Computer Science* **2018**, *131*, 511.

[5] L. Li, P. Gong, D. Sheng, S. Wang, W. Wang, X. Zhu, X. Shi, F. Wang, W. Han, S. Yang, K. Liu, H. Li, T. Zhai, *Advanced Materials* **2018**, *30*, 1804541.

[6] F. Liu, S. Zheng, X. He, A. Chaturvedi, J. He, W. L. Chow, T. R. Mion, X. Wang, J. Zhou, Q. Fu, H. J. Fan, B. K. Tay, L. Song, R. He, C. Kloc, P. M. Ajayan, Z. Liu, *Adv Funct Materials* **2016**, *26*, 1169.

[7] S. Rezaei-Mazinani, A. I. Ivanov, C. M. Proctor, P. Gkoupidenis, C. Bernard, G. G. Malliaras, E. Ismailova, *Adv Materials Technologies* **2018**, *3*, 1700333.

[8] V. Gruev, R. Perkins, T. York, *Opt. Express* **2010**, *18*, 19087.

[9] A. Altaqui, P. Sen, H. Schrickx, J. Rech, J.-W. Lee, M. Escuti, W. You, B. J. Kim, R. Kolbas, B. T. O'Connor, M. Kudenov, *Sci. Adv.* **2021**, *7*, eabe3196.

[10] J. S. Tyo, D. L. Goldstein, D. B. Chenault, J. A. Shaw, *Appl. Opt., AO* **2006**, *45*, 5453.

[11] P. Sen, R. Yang, J. J. Rech, Y. Feng, C. H. Y. Ho, J. Huang, F. So, R. J. Kline, W. You, M. W. Kudenov, B. T. O'Connor, *Advanced Optical Materials* **2019**, *7*, 1801346.

[12] H. M. Schrickx, P. Sen, R. E. Booth, A. Altaqui, J. Burleson, J. J. Rech, J. Lee, M. Biliroglu, K. Gundogdu, B. J. Kim, W. You, M. W. Kudenov, B. T. O'Connor, *Adv Funct Materials* **2022**, *32*, 2105820.

[13] M. Pandey, N. Kumari, S. Nagamatsu, S. S. Pandey, *J. Mater. Chem. C* **2019**, *7*, 13323.

[14] X. Luo, Y. Xue, J. Wu, W. Cai, D. Täuber, I. Malovicho, B. Sava, G. Cen, X. Lu, C. Zhao, I. G. Scheblykin, J. Yu, W. Mai, F. Liu, E. Wang, L. Hou, *Applied Physics Letters* **2022**, *121*, 233301.

[15] B. Park, Y. H. Huh, J. C. Shin, *Solar Energy Materials and Solar Cells* **2011**, *95*, 3543.

[16] R. Zhu, A. Kumar, Y. Yang, *Advanced Materials* **2011**, *23*, 4193.

[17] H. M. Schrickx, P. Sen, R. E. Booth, A. Altaqui, J. Burleson, J. J. Rech, J. Lee, M. Biliroglu, K. Gundogdu, B. J. Kim, W. You, M. W. Kudenov, B. T. O'Connor, *Adv Funct Materials* **2022**, *32*, 2105820.

[18] Y. Lin, J. Wang, Z. Zhang, H. Bai, Y. Li, D. Zhu, X. Zhan, *Advanced Materials* **2015**, *27*, 1170.

[19] S. Dai, T. Li, W. Wang, Y. Xiao, T. Lau, Z. Li, K. Liu, X. Lu, X. Zhan, *Advanced Materials* **2018**, *30*, 1706571.

[20] K. Gao, S. B. Jo, X. Shi, L. Nian, M. Zhang, Y. Kan, F. Lin, B. Kan, B. Xu, Q. Rong, L. Shui, F. Liu, X. Peng, G. Zhou, Y. Cao, A. K. -Y. Jen, *Advanced Materials* **2019**, *31*, 1807842.

[21] J. Yang, Y. Geng, J. Li, B. Zhao, Q. Guo, E. Zhou, *J. Phys. Chem. C* **2020**, *124*, 24616.

[22] G. Kupgan, X. K. Chen, J. L. Brédas, *Materials Today Advances* **2021**, *11*, 100154.

[23] A. Perevedentsev, H. Mejri, L. A. Ruiz-Preciado, T. Marszalek, U. Lemmer, P. W. M. Blom, G. Hernandez-Sosa, *Advanced Optical Materials* **2022**, *10*, 2102397.

[24] Y. Gao, J. Liao, H. Chen, H. Ning, Q. Wu, Z. Li, Z. Wang, X. Zhang, M. Shao, Y. Yu, *Advanced Science* **2023**, *10*, 2204727.

[25] A. S. M. Tripathi, R. K. Gupta, S. Sharma, S. Nagamatsu, S. S. Pandey, *Organic Electronics* **2020**, *81*, 105687.

[26] J. Yuan, Y. Zhang, L. Zhou, G. Zhang, H.-L. Yip, T.-K. Lau, X. Lu, C. Zhu, H. Peng, P. A. Johnson, M. Leclerc, Y. Cao, J. Ulanski, Y. Li, Y. Zou, *Joule* **2019**, *3*, 1140.

[27] Y. Xie, C. Zhou, X. Ma, S. Y. Jeong, H. Y. Woo, F. Huang, Y. Yang, H. Yu, J. Li, F. Zhang, K. Wang, X. Zhu, *Advanced Energy Materials* **2024**, *14*, 2400013.

[28] Z. Lou, J. Tao, B. Wei, X. Jiang, S. Cheng, Z. Wang, C. Qin, R. Liang, H. Guo, L. Zhu, P. Müller-Buschbaum, H. Cheng, X. Xu, *Advanced Science* **2023**, *10*, 2304174.

[29] H. Shi, R. Xia, G. Zhang, H. Yip, Y. Cao, *Advanced Energy Materials* **2019**, *9*, 1803438.

[30] U. Zhokhavets, G. Gobsch, H. Hoppe, N. S. Sariciftci, *Synthetic Metals* **2004**, *143*, 113.

[31] A. Perevedentsev, H. Mejri, L. A. Ruiz-Preciado, T. Marszalek, U. Lemmer, P. W. M. Blom, G. Hernandez-Sosa, *Advanced Optical Materials* **2022**, *10*, 2102397.

[32] D. Kroh, F. Eller, K. Schötz, S. Wedler, L. Perdigón-Toro, G. Freychet, Q. Wei, M. Dörr, D. Jones, Y. Zou, E. M. Herzig, D. Neher, A. Köhler, *Adv Funct Materials* **2022**, *32*, 2205711.

[33] E. K. Miller, G. S. Maskel, C. Y. Yang, A. J. Heeger, *Phys. Rev. B* **1999**, *60*, 8028.

[34] L. Yu, D. Qian, S. Marina, F. A. A. Nugroho, A. Sharma, S. Hultmark, A. I. Hofmann, R. Kroon, J. Benduhn, D.-M. Smilgies, K. Vandewal, M. R. Andersson, C. Langhammer, J. Martín, F. Gao, C. Müller, *ACS Appl. Mater. Interfaces* **2019**, *11*, 21766.

[35] Z. Wang, K. Gao, Y. Kan, M. Zhang, C. Qiu, L. Zhu, Z. Zhao, X. Peng, W. Feng, Z. Qian, X. Gu, A. K.-Y. Jen, B. Z. Tang, Y. Cao, Y. Zhang, F. Liu, *Nat Commun* **2021**, *12*, 332.

[36] M. Ghasemi, H. Hu, Z. Peng, J. J. Rech, I. Angunawela, J. H. Carpenter, S. J. Stuard, A. Wadsworth, I. McCulloch, W. You, H. Ade, *Joule* **2019**, *3*, 1328.

[37] M. Xiao, B. Kang, S. B. Lee, L. M. A. Perdigão, A. Luci, D. A. Warr, S. P. Senanayak, M. Nikolka, M. Statz, Y. Wu, A. Sadhanala, S. Schott, R. Carey, Q. Wang, M. Lee, C. Kim, A. Onwubiko, C. Jellett, H. Liao, W. Yue, K. Cho, G. Costantini, I. McCulloch, H. Sirringhaus, *Advanced Materials* **2020**, *32*, 2000063.

[38] W. A. Memon, R. Zhou, Y. Zhang, Y. Wang, L. Liu, C. Yang, J. Zhang, A. Liaqat, L. Xie, Z. Wei, *Adv Funct Materials* **2022**, *32*, 2110080.

[39] A. S. M. Tripathi, M. Pandey, S. Sadakata, S. Nagamatsu, W. Takashima, S. Hayase, S. S. Pandey, *Applied Physics Letters* **2018**, *112*, 123301.

[40] D. Niedzialek, V. Lemaur, D. Dudenko, J. Shu, M. R. Hansen, J. W. Andreasen, W. Pisula, K. Müllen, J. Cornil, D. Beljonne, *Advanced Materials* **2013**, *25*, 1939.
[41] J. Fidyk, W. Waliszewski, P. Sleczkowski, A. Kiersnowski, W. Pisula, T. Marszalek, *Polymers* **2020**, *12*, 2662.
[42] Z. Zhang, X. Ma, J. Zhong, *Nat Commun* **2015**, *6*, 6225.
[43] L. Tong, X. Huang, P. Wang, L. Ye, M. Peng, L. An, Q. Sun, Y. Zhang, G. Yang, Z. Li, F. Zhong, F. Wang, Y. Wang, M. Motlag, W. Wu, G. J. Cheng, W. Hu, *Nat Commun* **2020**, *11*, 2308.